CFD ANALYSIS OF A POLYBUTENE REACTOR TO DIAGNOSE CAUSES OF POLYMER ADHESION AT INNER WALLS

D. RAMAJO†, M. RAVICULÉ‡, G. HOROWITZ‡, M. STORTI† and N. NIGRO†

†*International Center for Computational Methods in Engineering (CIMEC)*
INTEC-UNL-CONICET, Güemes 3450, Santa Fe, Argentina
dramajo@ceride.gov.ar
‡ Centro de Tecnología Argentina (CTA), Repsol-YPF, Baradero s/nro. 1925, Ensenada, Argentina
mravicules@repsolypf.com

***Abstract*— In this work the flow patterns inside a polybutene reactor were studied by CFD (Computational Fluid Dynamics) using finite elements. Research was carried out with the aim to find possible causes of excessive adhesion of polymer and catalyst particles at the reactor inner walls. The multi-fluid formulation for a three-phase system formed by liquid reactor mixture, solid catalyst particles and small gas bubbles generated by the reaction was applied. Deposition of solid particles and a non-homogeneous flow distribution over the lower reactor walls were founded. Based on the hypothesis that adhesion phenomena is related to a combination of catalyst-particle precipitation at walls and locally low shear stresses, several operative and constructive modifications were proposed in order to reduce this phenomenon.**

***Keywords*— polybutene reactor, CFD, adhesion.**

I. INTRODUCTION

Polybutenes are manufactured from C_4 olefin refinery streams of fluidized catalytic crakings. The polimerization is catalised by traces of water and $AlCl_3$. The polybutene reactor under study is a tri-phase tank. The solubility of $AlCl_3$ in the reaction mixture is low which originates the presence of solid particles in the reactor. The heat of reaction is partialy disipated by ebullition of the reaction mixture generating the gas phase. A more detailed description of the process can be found in (Kennedy and Marechal, 1991).

Polymerization takes place around catalyst particles. If reactions occur close to the reactor walls, catalyst particles surrounded by polymer may stick forming large clusters which after a few seconds will be hardly adhered to the walls. Once deposits are formed they are very difficult to remove, reducing the operative capacity of the reactor. Adhesion process is continuous and deposits only can be removed by chemical or mechanical techniques. In the reactor under study, the rate of adhesion is faster enough to reduce a very important part of the overall reactor volume after a few years. This fact forces to stop the plant frequently in order to clean the reactor walls, with the consequent high economical impact.

The reactor analyzed does not have any impeller and its charge is only mixed by continuous recirculation forced by pumping the emulsion from the reactor outlet located upwards and introducing again through the reactor entrance located at the bottom.

In order to gain some insight about the performance of this equipment it is advisable to know how the feed flows inside the reactor, determining residence times, local shear stresses, catalyst particles concentration among others. With such information it is possible to image how should be the possible scenario of polymer adhesion.

In this work a finite element CFD analysis of the flow patterns inside the reactor is presented. Inspired about these computational results feasible operative and constructive modifications are proposed, based on the assumption that adhesion is closely related to a combination of catalyst particle deposition (precipitation) and low enough wall shear stresses. In general CFD results are nowadays being used as a very useful design tool. In the reactor design area this technology has not been massively employed being this contribution an example about how this methodology serves to the designer to improve the process productivity.

II. METHODS

A. Problem definition. Constructive and operative features

Polybutene (PIB) reactor is a cylindrical vessel with a total height of 9.5 m, a diameter of 3.3 m and an approximate volume of 60 m^3. In Fig. 1 the main constructive data of the reactor are showed. Fig. 1 also shows the dimensions and locations of the inlet and outlet ducts. It is remarkable the sharp curvature of the inlet duct located at the bottom of the vessel.

Reactor is made of carbon steel and has a thermal insulating layer on its outer side. Reactor has not any mechanical impeller, so in order to enhance the reaction process the emulsion is continuously re-circulated. During the catalytic reaction the isobutylene is polymerized producing molecular weights depending on process temperature catalysts concentration and reaction mixture composition.

Fig. 2 is part of a flow sheet and it is useful to clarify the main fluxes involved on the process. Re-circulation

is done by pumping the charge from the *Outlet A* to the *Inlet A* at the bottom side. At the same time, a vapor stream is collected through the *Outlet B* at the top of the PIB reactor and the liquid charge, formed by the polymer diluted in the C4 mixture, is extracted through two small ducts at the *Outlet C*. Small quantities of catalyst are drifted through the outlet C. Therefore, both compounds must be made up through an auxiliary *inlet B*.

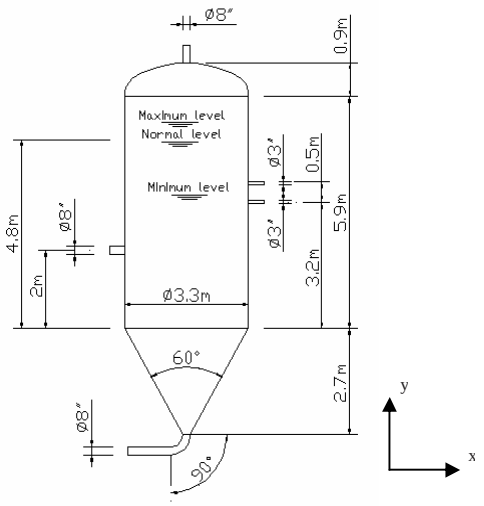

Fig. 1. x-y view of the PIB reactor. Main dimensions.

As it is sketched in Fig. 2 three phases are present, the emulsion formed by the reaction solution (liquid phase), small vapor bubbles (gaseous phase) and small catalyst particles (solid phase). C4 mixture bubbles are generated by an exothermic reaction consuming isobutylene. Due to the necessity to control polymer molecular weght, the temperature and pressure conditions should be strictly controlled, varying from -1ºC and 1.21 atm to 25ºC and 3 atm respectively. Besides, an average catalyst concentration of 0.3 kg per m^3 of emulsion is required in order to perform the polymerization process.

In table 1 the rheological properties of the different phases involved are listed for numerical simulation purposes. Since overall operation temperature needs to be kept almost constant, an isothermal hypothesis is adopted for modeling the process, so only the transport properties of phases are relevant.

Catalyst particle sizes vary from less than 50 microns (20% of the total amount of particle) to more than 500 microns (6% of the total particle inventory). But particle size distribution can be roughly divided in two groups; the first one containing particles of 65 microns and the second one comprising particles of around 140 microns, corresponding to 34% and 35% of the total particle inventory respectively.

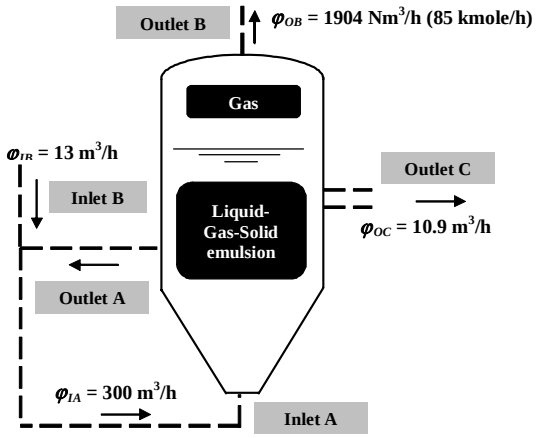

Fig. 2. Layout of part of the process.

Particle size has a remarkable influence on drag forces. Small particles are easier drifted by the mean flow than large ones. In addition, considering more than one particle size involves a high computational cost (mass and momentum equations for each particle size must be solved in each computational cell). For these reasons, a unique particle size was chosen to represent the whole range of particle sizes, taking into account the higher decantation velocity of the second particle group (about 0.1 m/s) respect to the first one (about 0.0125 m/s).

Table 1. Rheological properties of the three phases. [(A)] Refer to 292.3K and 1.1 atm, [(B)] Refer to 258K and 1 atm, [(C)] Refer to 253K and 1 atm.

	Phase		
	Liquid	Gas	Solid
Denomination	Reaction mixture	vapor	aluminum trichloride
Assumed shape for modeling	continuous	Continuous/ bubbles	Spheres
Characteristic size	--	1 mm to 2 mm	50 μ to 140 μ
Density (kg/m^3)	690[(A)]	3.15[(A)]	2440
Viscosity (centistokes)	2,0705[(B)] - 2,2459[(C)]	1,64[(A)]	--

As regard the gaseous phase, it is generated during the polymerization reaction in the vicinity of catalyst particles. As was observed in an experimental reactor, the reaction produces small bubbles of C4 of about 1 to 2 mm, which move upward reaching the emulsion free surface.

As for the liquid phase, a sample was extracted from the reactor in order to characterize its transport properties. The emulsion kinematic viscosity for two temperatures was measured at laboratory (see table 1) and the corresponding values at process temperatures were estimated by logarithmical extrapolation using the following expression:

$$\mu = \frac{\rho}{1000}\left[a\ln(T)+b\right], \tag{1}$$

being *a* and *b* obtained by fitting as -8.96 and 51.84 respectively.

B. Mathematical model

The unsteady multi-fluid formulation was employed for simulation. In this formulation, Navier-Stokes equations are modified in order to introduce the volume fraction of each phase in the mixture along with appropriate terms considering the mass, momentum and energy transferred through the interface among phases. The continuity equation for each α phase is the following:

$$\frac{\partial(\delta_\alpha\rho_\alpha)}{\partial t} + \nabla\bullet\left(\delta_\alpha\rho_\alpha\vec{U}_\alpha\right) = S_\alpha + \Gamma_{S\alpha} \text{ and } \sum_\alpha \delta_\alpha = 1, \tag{2}$$

where δ_α, ρ_α and $\vec{U}_\alpha$ are the volume fraction, density and velocity vector of the α phase. S_α are volumetric mass sources or sinks and $\Gamma_{S\alpha}$ are mass flows through the interfaces between α and the others phases. It is important to note the role of the constraint Eq. (2).

Momentum equation for α phase was written as:

$$\frac{\partial}{\partial t}\left(\delta_\alpha\rho_\alpha\vec{U}_\alpha\right) + \nabla\bullet\left(\delta_\alpha\left(\rho_\alpha\vec{U}_\alpha\otimes\vec{U}_\alpha\right)\right) = -\delta_\alpha\nabla P + \nabla\bullet\tau_\alpha + \varphi_\alpha + M_\alpha + \Gamma_{M\alpha}, \tag{3}$$

where *P* is the static pressure shared by all the phases (one pressure model), τ_α is the shear stress tensor, M_α are the volumetric external momentum sources (potential force fields, eg. gravity), $\Gamma_{M\alpha}$ are interface forces caused by the presence of others phases (eg. drag and lift) and φ_α are the net momentum quantities transferred at the α phase by mass transfer through its interface. Although Eq. (2) and (3) have been formulated for fluid continuous phases, they can also be employed to describe solid and gas dispersed phases as in this case for catalyst particles and C4 bubbles. The assumption that dispersed particle phases behave like fluids continuous is valid only for low phase volume fractions. In these cases, the shear stress tensor τ_α for dispersed phases gets negligible in relation with interface forces $\Gamma_{M\alpha}$. Otherwise for solid dispersed phases with high solid volume fractions (upper than 0.1) kinetic and granular theories must be incorporated in order to modeled the shear stress tensor τ_α. Besides, an additional solid pressure must be considered (Ranade, 2002; Enwald et al., 1996; Srivastava and Sundaresan, 2003; Makkawi and Ocone, 2003; Gidaspow et al., 2004). For the liquid continuous phase the stress tensor is defined as:

$$\tau_{RM} = \mu_{RM}^{eff}\left(\nabla\vec{U}_{RM} + \nabla\vec{U}_{RM}{}^{T}\right), \tag{4}$$

with μ_{RM}^{eff} the effective dynamic viscosity of the reaction mixture, it means the molecular one modified by the turbulence contribution. Large eddy simulation with a simple Smagorinsky model (Smagorinsky, 1963; Wilcox, 1998) is employed to model the turbulence effects. This eddy viscosity model is defined as:

$$\begin{aligned}\mu_{RM}^{eff} &= \rho_{RM}\,\nu_{RM}^{eff}\\ \nu_{RM}^{eff} &= (C_S h)^2 D\sqrt{\varepsilon:\varepsilon}\\ \varepsilon &= \frac{1}{2}\left(\nabla U + \nabla U^T\right)\end{aligned}, \tag{5}$$

with ρ_{RM} the reaction mixture density, $C_S = 0.18$ the Smagorinsky constant, h the spatial discretization size, *D* a Van-Driest damping factor to correct the influence of the wall proximity and ε the deformation rate tensor.

Focusing on the system, it is composed by the reaction mixture (continuous fluid), vapor (dispersed fluid bubbles) and catalyst (dispersed solid particles). For low particle volume fractions the bubble-particle contact is negligible thus shear stress term in Eq. (3) is not taken into account. C4-bubble generation can be incorporated either as a transferred mass quantity through interfaces (from reaction mixture to dispersed fluid bubbles) or as a volumetric mass source (for dispersed fluid bubbles) along with a volumetric mass sink (for reaction mixture). Taking into account the relationship between vapor generation and catalyst particles, implementing the second option seems to be easier than the first one. Therefore, $\Gamma_{S\alpha} = 0$ in Eq. (2) and the following local expressions for the mass source $S_{vapor}(x)$ and the mass sink $S_{RM}(x)$ were used:

$$S_{vapor}(x) = \frac{\varphi_{OB}}{V_{emul}}\frac{\delta_{cat}}{\delta_{cat}^0}, \qquad S_{RM}(x) = -S_{vapor}(x). \tag{6}$$

In Eq. (6) φ_{OB} is the total mass flow of C4 through *Outlet B*, V_{emul} is the total emulsion volume and δ_{cat} and δ_{cat}^0 are the local and averaged catalyst volume fractions.

As for the momentum equation, momentum transfer due to mass exchange through interfaces was taken null ($\Gamma_{M\alpha} = 0$) and interface forces M_α were only given

by drag efforts. Because of the low volume concentration of solid particles the Schiller-Naumann model was suitable to estimate their drag coefficient C_D. As for the C4 bubbles, the volume fraction of this phase was a priori unknown so the same drag model was implemented for its. C_D was expressed as a function of the particle Reynolds number Re_p as:

$$C_D = \begin{cases} \dfrac{24}{\mathrm{Re}_P}\left(1+0.15\,\mathrm{Re}_P{}^{0.687}\right) & if \quad \mathrm{Re}_P < 1000 \\ 0.44 & if \quad 1000 < \mathrm{Re}_P < 2e5 \end{cases} \qquad (7)$$

.

C. Numerical formulation

The mathematical model defined by Eq. (2)-(7) is discretized by stabilized finite elements according to the following formulation. Let the functional spaces be:

$$\begin{aligned} S_v^h &= \left\{ v^h \mid v^h \in \left(H^{1h}\right)^{nsd}, v^h \equiv v_D^h \ in\ \Gamma_D \right\} \\ S_p^h &= \left\{ q^h \mid q^h \in H^{1h} \right\} \\ S_\delta^h &= \left\{ r^h \mid r^h \in H^{1h}, r^h \equiv r_D^h \ in\ \Gamma_D \right\} \\ V_v^h &= \left\{ N_v^h \mid N_v^h \in \left(H^{1h}\right)^{nsd}, N_v^h \equiv 0 \ in\ \Gamma_D \right\} \\ V_p^h &= S_p^h \\ V_\delta^h &= \left\{ N_\delta^h \mid N_\delta^h \in \left(H^{1h}\right), N_\delta^h \equiv 0 \ in\ \Gamma_D \right\} \end{aligned} \qquad (8)$$

$$H^{1h} = \left\{ \phi^h \mid \phi^h \in C^0\left(\overline{\Omega}\right), \phi^h\big|_{\Omega^e} \in P^1, \forall \Omega^e \in \Im \right\}$$

with H^{1h} the Sobolev space of order one, $\Im$ the mesh partition, Ω the computational domain, Γ its boundary and $\overline{\Omega}$ its closure, Γ_D the part of the boundary with Dirichlet boundary conditions and *nsd* the number of spatial coordinates. *S* is used for the trial functions (interpolation) and *V* for the weight functions. The finite element problem is defined as:

find $\delta_\beta^h \in S_\delta^h$, $\vec{U}_\beta^h \in S_v^h$, $p^h \in S_p^h$, $\vec{U}_C^h \in S_v^h$ with β an index over the dispersed phases and *C* the index of the continuous phase such that

$$\begin{aligned} &\sum_\alpha \int_\Omega W_{CONT}^\alpha \left[\frac{\partial(\delta_\alpha \rho_\alpha)}{\partial t} + \nabla \bullet (\delta_\alpha \rho_\alpha \bar{U}_\alpha) - (S_\alpha + \Gamma_{S\alpha}) \right] d\Omega \ + \\ &+ \sum_\alpha \int_\Omega W_{MOM}^\alpha \left[\begin{array}{l} \dfrac{\partial}{\partial t}(\delta_\alpha \rho_\alpha \bar{U}_\alpha) + \nabla \bullet (\delta_\alpha (\rho_\alpha \bar{U}_\alpha \otimes \bar{U}_\alpha)) + \\ \delta_\alpha \nabla P - \left(\nabla \bullet \tau_\alpha + \varphi_\alpha + M_\alpha + \Gamma_{M\alpha}\right) \end{array} \right] d\Omega \ = 0 \end{aligned} \qquad (9)$$

$$\forall W_{CONT}^\alpha \in V_{CONT}^\alpha \ , \forall W_{MOM}^\alpha \in V_{MOM}^\alpha \ , \forall\, \alpha \quad ,$$

with α each phase (continuous and dispersed) in the system. The weight residual formulation (9) uses different weight functions for each equation (CONT: for continuity equations and MOM: for momentum equations) according to numerical stabilization requirements (Tezduyar et al., 1992; García-Cascales and Paillère, 2006; Zanotti, 2007). As regard the continuity equations, the continuous phase ($\alpha = C$) uses $V_{CONT}^C = V_p^h$ and each dispersed phase ($\alpha = \beta$) uses $V_{CONT}^\beta = V_\delta^h$. As for the momentum equations, both the continuous phase and each dispersed one use $V_{MOM}^\alpha = V_v^h$.

D. Numerical model

In order to gain some insight about the role of the free surface located between the reaction mixture and the vapor existing in the upper part of the reactor the first simulation was done using the overall reactor geometry (see Fig. 1). These preliminary results showed that emulsion free surface had a motion negligible. Hence for the rest simulations only a fraction of the reactor above the normal level of the emulsion free surface (around 0.4 m) was taken into account, reducing the mesh size in 20%. Regarding to the spatial discretization the computational domain was partitioned in 200,716 tetrahedrons and a local refinement was employed around inlet and outlet ducts. Due to the small temperature variations the problem was considered as isothermal and simulations were performed at two operation temperatures corresponding to the operation extreme conditions of -1ºC and 25ºC respectively, considering the corresponding reaction mixture viscosities.

Regarding to the time integration a first order backward Euler scheme was applied. For each analyzed case a time period of 200 seconds with a constant time step of 0.01 seconds was simulated. The problem was solved using distributed computing over several processors in a Beowulf cluster (Storti et al.; Sonzogni et al., 2002). Each simulation (20,000 time steps) demanded around 5 days in a Beowulf Cluster with 10 processors.

Boundary conditions. Fully developed velocities were imposed to Inlet A, Outlet A and Outlet B while a constant pressure equal to the operation pressure was employed at Outlet C. In order to modeling re-circulation flow from Outlet A to Inlet A the volume fraction for each phase at Inlet A must be linked to the outgoing mass flow at Outlet A. It means that the instantaneous mass flow rate of each phase at Outlet A along with the corresponding from Inlet B (constant volume fractions of δ_{cat} = 1.24e-4, δ_{vapor} = 0 and δ_{RM} = 0.999876) were added in order to estimate the composition of the entering flow. Moreover, mass flow rate at each boundary were monitored during the whole simulation time interval, guarantying the reactor global mass conservation, focusing the effort in fitting the vapor generation with the volumetric flow rate data measured at Outlet C. The velocity for each phase at walls was considered as non slip.

E. Results and discussion

As it was before mentioned two operation conditions were simulated. The first one corresponding to a con-

stant temperature of -1ºC and a pressure of 1.21 atmospheres at the top part of the reactor, and the second one for 25ºC of temperature and 3 atmospheres of pressure. In the following paragraphs the results for the first operation condition are extensively discussed. A steady state solution was assumed after the global mass balance was verified. As it was previously mentioned, adhesion problem was assumed to be related to the catalyst concentration at the reactor walls as well as to local low wall-shear stresses. Attending these assumptions the catalyst volume fractions (CVF) along with the wall shear efforts (WSE) at cross-sectional mean planes and at reactor walls are displayed in Fig. 3.

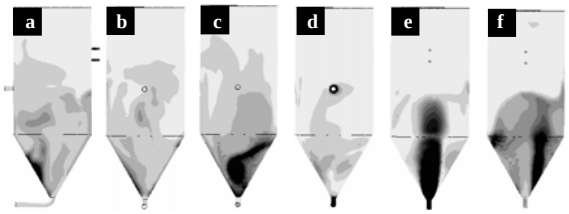

Fig. 3. CVF (scale range from 0 to 8x10-4) and WSE (scale range from 0 to 1.0) at t = 200 seconds. From left to right: a) CVF at mean plane x-y. b) CVF at mean plane y-z. c) CVF at reactor walls from –x view. d) WSE at reactor walls from –x view. e) CVF at reactor walls from x view. f) WSE at reactor walls from x view.

Fig. 3 contains six pictures, the first two of them are two cut planes, one an x-y cut plane where the entrance duct and the outlet ducts are cut in halves. The other one is perpendicular to the first one and it is placed on the y-z plane. This view is called the front view while the opposite one is called the rear view. The four remaining pictures show the front (third and fourth pictures) and rear side walls (the fifth and sixth ones). These figures show the conical part of the reactor receiving the fluid flow from the entrance duct and due to its inclination of about sixty degree, this part is prone to particle adhesion. Therefore, most of the attention will be given to this part of the reactor geometry.

In Fig. 3-a it is clearly noted how the entrance flow jet has a strong tangential velocity component, sweeping the cone right wall and allowing the decantation of solid particles at the opposite wall. A particle concentration larger than the averaged one ($1.24x10^{-4}$) is visualized over most of the reactor cone, whereas a small part of this region that is directly affected by the entrance flow jet holds lower particle concentrations. In Fig. 4 both CVF and WSE over the conical reactor walls are drawn at three different simulation times. It is useful to see how the entrance jet comes into the reactor sweeping a fraction of the conical wall with a period of around 30 seconds. Results in Fig. 4 show that decantation of solid particles over the reactor lower walls increases catalyst concentration above 3 times respect to the averaged concentration. Lower catalyst concentrations are founded at the entrance-jet core, while regions with volume fractions greater than $4x10^{-4}$ are located in the vicinity of it.

Results showed a periodic behavior of the flow jet like a wandering effect. This fact motivated that results were time averaged along a time period of 140 seconds in order to capture the mean-flow characteristics. Due to this fact, more than 150 mesh sampling points over the reactor cone were selected and 140 solutions at different time steps were considered. In Fig. 5 the minimum, maximum and time-averaged values for CVF and WSE at four radial distances from the entrance are drawn (see sketch in figure 8 for radial coordinate definition). Polar diagrams in Fig. 5 underline the zone directly influenced by the entrance flow. The increment in CVF on the opposite conical wall is also evidenced. As it can be seen, close to the entrance (radius = 0.25 m), CVF reaches $6x10^{-4}$ on the left-middle conical wall while minimum values are around $4x10^{-4}$. WSE excesses 6 Pa in a direction aligned with the jet (0 degrees at polar diagram) and close to the entrance orifice, but it quickly diminishes along the radial coordinate. Both CVF and WSE become more homogeneous while radius grows. Furthermore, maximum CVF decreases, although the averaged one holds close to $4x10^{-4}$. WSE quickly diminishes far away from the entrance and the efforts hardly ever excess 1 Pa for radius larger than 1.42 m.

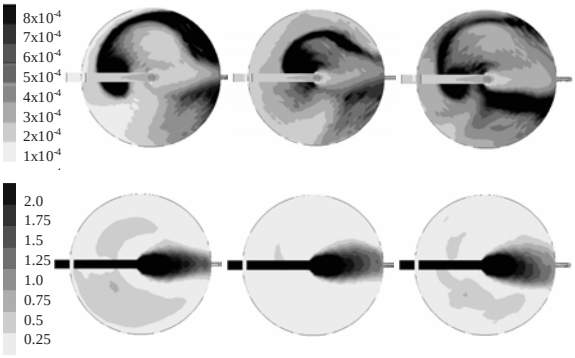

Fig 4. Conical reactor walls (view from the bottom). *Upper:* catalyst volume fraction (CVF). *Bottom:* wall shear efforts (WSE). *Left: t* = 120 secs. *Center: t* = 150 secs. *Right: t* = 200 secs.

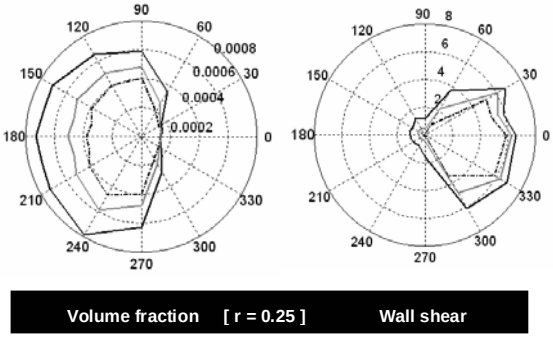

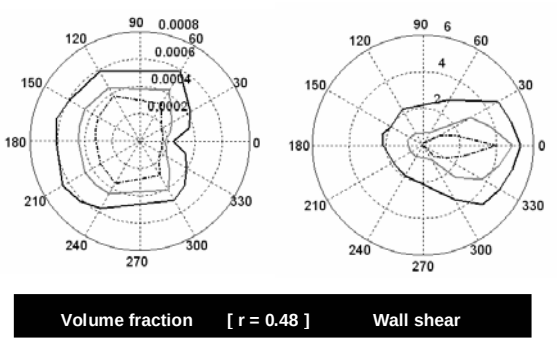

Fig 5. Conical reactor walls. Maximum (solid black line), minimum (dotted-dashed black line) and averaged (solid gray line) values for catalyst volume fraction (CVF) and wall shear efforts (WSE) at different radius.

By changing the operation conditions from -1ºC to 25ºC of temperature the viscosity was reduced from 1.112 centistokes to 0.547 centistokes. Viscosity reduction affects directly wall shear efforts as well as drag forces, lessening both of them. This fact increases decantation over the conical reactor walls indicating that higher operation temperatures would promote higher adhesion rates.

F. Studied modifications

Three operative and constructive modifications are discussed and they are assessed in terms of particle decantation reduction and wall shear stresses increment.

First case: an increased re-circulation flow. The first case analyzed is defined in terms of an increment of the recirculation flow from 288m^3/h to 400 m^3/h holding the original constructive geometry. In this case flow-pattern results are similar to those founded for the lower re-circulation flow. This means that the entering flow jet comes into the reactor producing the same non-homogeneous flow distribution over the conical walls. Fig. 6 draws the maximum (roof limit) and minimum (floor limit) extreme values of CVF and WSE over the conical reactor walls for different radius. Min roof refers to the maximum value (roof limit) of the minimum CVF while Min floor refers to the minimum one (floor limit). This means that any minimum CVF value is bounded between Min floor and Min roof curves. As it can be noted, minimum CVF values are reduced as re-circulation flow increases. On the other hand, maximum CVF values do not show any significant difference for both analyzed flows. Fig. 7 displays the same analysis for WSE. Minimum and maximum WSE quickly fall down along the radius. There are not significant differences in floor limits for maximum and minimum WSE by increasing the re-circulation flow. As regard the roof-limit of minimum WSE, it is strongly increased near the entrance but differences become negligible beyond radius of about 0.7 m. On the other hand, significant differences are founded for the roof-limit of maximum WSE at every radius.

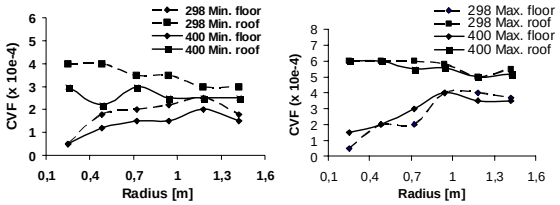

Fig. 6. Roof and floor limits for the maximum and minimum CVF over the conical reactor walls for both analyzed re-circulation flows. Left: minimum CVF range. Right: maximum CVF range.

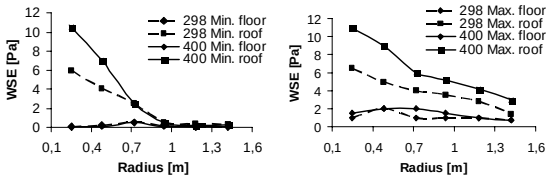

Fig. 7. Roof and floor limits for the maximum and minimum WSE over the conical reactor walls for both analyzed re-circulation flows. Left: minimum WSE range. Right: maximum WSE range.

As it can be noted from Fig. 6 and 7, re-circulation-flow enlargement has a positive effect in both CVF and WSE. Nevertheless, since entrance flow keeps strongly channeled over a fraction of the overall conical reactor wall, the inlet elbow must be modified in order to promote the angular homogenization of the entrance mass flow rate. In the next analyzed case, the inlet elbow is removed and a deflector is incorporated inside the reactor in order to get a more homogeneous distribution of the entering flow over the conical reactor walls.

Second case: removal of the inlet elbow and incorporation of a flow deflector. Fig. 8 shows the constructive modifications implemented around the flow-entrance zone. The inlet elbow was replaced by a straight duct. Furthermore, a solid rhomboidal deflector with a total height of 0.7 m was incorporated. The rhomboidal deflector was located as close as possible to the conical reactor walls avoiding obstructions during the reactor normal operation. According to information about the maximum catalist particle size two positions were considered, the first one with a gap of 30 mm and a second one with a gap of 20 mm. Simulations were performed considering a re-circulation flow of 400 m^3/h.

The results obtained allow conclude that the included modifications strongly affect the entering flow jet producing a more homogeneous CVF and WSE distribution over the conical reactor wall. In Fig. 9 and 10 the maximum and minimum limits for CVF and WSE are drawn for both deflector positions.

In Fig. 9 the roof and floor limits for maximum and minimum CVF are drastically reduced around the gap zone. Once the flow leaves this region, CVF increases

meaningfully. Furthermore, differences between roof and floor limits for maximum and minimum CVF become smaller.

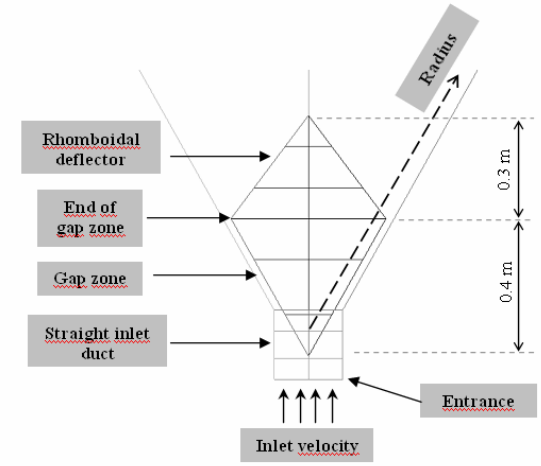

Fig. 8. Removal of the inlet elbow and incorporation of a rhomboidal deflector.

In fact, hence flow distribution gets more homogeneous the maximum and minimum limits approach themselves. WSE and CVF have an opposite behavior along gap zone. This means that WSE diminishes while CVF increases for the first 0.7 m, after that, both become roughly constants.

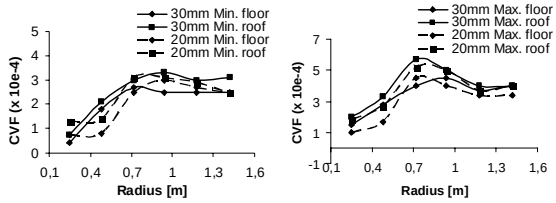

Fig. 9. Roof and floor limits for the maximum and minimum CVF over the conical reactor walls for both analyzed deflector locations. Left: minimum CVF range. Right: maximum CVF range.

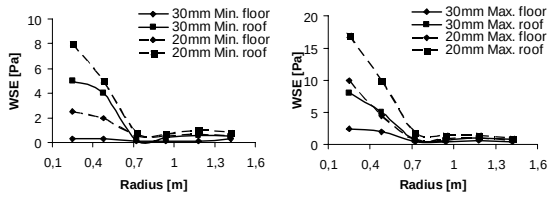

Fig. 10. Roof and floor limits for the maximum and minimum WSE over the conical reactor walls for both analyzed deflector locations. Left: minimum WSE range. Right: maximum WSE range.

As regard the wall shear efforts, both minimum and maximum WSE are strongly increased by reducing the gap but WSE quickly diminishes far away from the gap zone. By comparing Fig. 7 and 10 differences between the roof and floor limits get smaller for the second case, as a consequence of the more homogeneous flow pattern around the entrance.

As it was pointed out, removing the inlet elbow clearly improves the inlet-flow distribution. Therefore, several constructive modifications for the inlet duct were studied in order to promote this behavior. Due to the actual constructive characteristics of the PIB reactor all possible modifications were constrained to have a limit height from the ground level to the reactor entrance equal to 1.0 m. Four inlet configurations were considered; the first one by lowering the duct 0.6 m, the second and thirst ones by incorporating stagnation deposits of lengths H = 0.7 m and 0.8 m, respectively, and the last one using a cyclonic configuration in order to get a rotational flow. Fig. 11 shows the original elbow along with the first, second and third configurations while Fig. 12 shows several views of the fourth model.

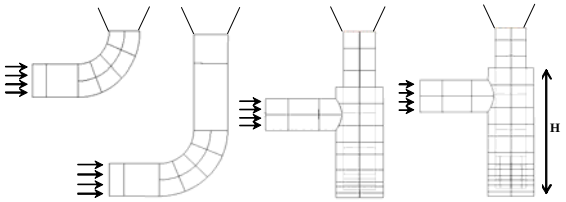

Fig. 11. From left to right: the original elbow, the extended one and the second and third configurations.

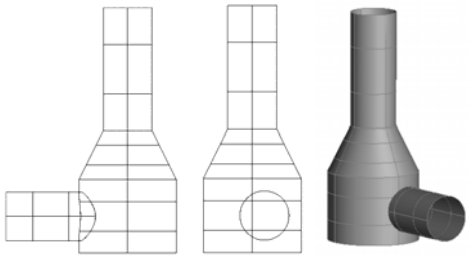

Fig. 12. Cyclonic elbow. *Left:* lateral view. *Center:* front view. *Right:* 3D perspective.

In order to find the best elbow model a fully developed turbulent velocity was introduced through the inlet while a constant pressure was considered at outlet. Once stationary conditions were reached the velocity field at outlet was analyzed. Fig. 13 shows the vertical velocity for all the considered models. As can be seen, the original elbow geometry produces a non homogeneous flow distribution at the downstream. The flow pattern does not become more homogeneous by extending the duct upstream. Of course, the latest is expected because the development length for this kind of flows is larger than the admissible duct extension (three times the duct diameter). As for the modified elbows involving a stagnation deposit, some improvement is obtained with the biggest one. Although the flow pattern is not homogeneous it seems to be more isotropic than the others.

As can be seen the results above showed not complete solve the current non-homogeneous flow distribution. On the other hand, as is displayed in Fig. 14 the fourth proposed elbow introduces a non-stationary rotational flow pattern wandering the overall duct cross area with a rotational period rounding 2 seconds.

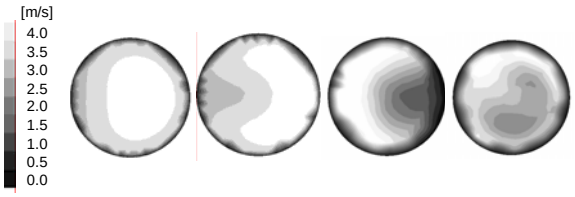

Fig. 13. Vertical velocity at outlet for the original, and the first, second and third analyzed elbows.

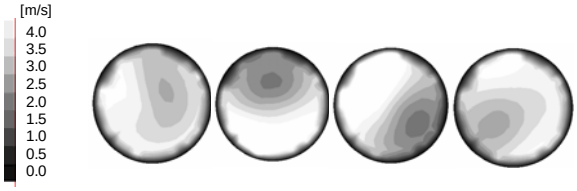

Fig. 14. Vertical velocity at outlet at four time states for the cyclonic elbow. From *left* to *right*: t = 0.5, 1, 1.5 and 2 seconds.

It must be noted that any constructive modification affecting the original reactor geometry could entail an oversize of the re-circulation pumps. In table 2 the estimation of the pressure lost for each analyzed elbow are included.

Table 2. Pressure lost generated by incorporating the analyzed constructive modifications (re-circulation flow of 400 m^3/h).

Constructive modification	Pressure lost ΔP [Pa]
Original elbow	-811
Extended elbow	-1169
Elbow with deposit of H = 0.70 m	-25458
Elbow with deposit of H = 0.80 m	-26077
Cyclonic elbow	-14484
Rhomboidal deflector (gap: 30 mm)	-2479
Rhomboidal deflector (gap: 20 mm)	-6727

From pressure lost in table 2 it is easy to have a rough estimation of the additional pump overload by adding the pressure lost of each constructive modification as follow:

$$\Delta P_{added} = \Delta P_{new\_elbow} + \Delta P_{deflector} - \Delta P_{old\_elbow}. \quad (10)$$

For instance, considering the incorporation of a cyclonic elbow along with a rhomboidal deflector with a gap of 20 mm, it would produces and additional pressure overload of 21,211 Pa.

Third case: incorporation of a gyratory spout for injecting the inlet flow. As it was mentioned for the previous cases, WSE strongly diminishes along the radius. For this reason, it was incorporated a gyratory spout spinning over the y-coordinate axis in order to inject the re-circulation flow. The object of it is producing a high velocity jet that sweeps the whole conical reactor wall during its rotation. In such a way, the inlet duct was removed from the model and the re-circulation mass flow rate was introduced into the reactor by a local mass and momentum source located at the bottommost point of the reactor cone.

A cylindrical spout of 50 mm of diameter was adopted and three injection velocities of 28, 41.1 and 56 m/s corresponding to entrance flows of 200, 300 and 400 m^3/h was considered. For the spout movement a constant rotational velocity of 10 revolutions per minute was applied for all flows.

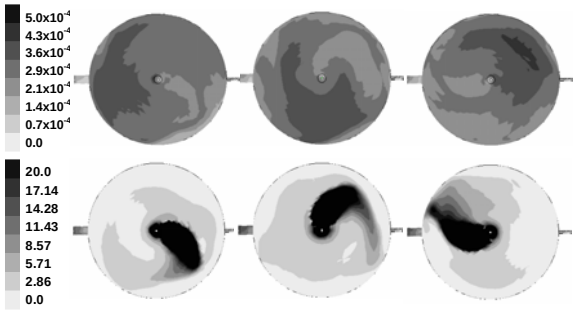

Fig. 15. Conical reactor walls (recirculation flow of 400 m^3/h). *Upper:* catalyst volume fraction (CVF). *Bottom:* wall shear efforts (WSE). *Left: t* = 126 seconds. *Center: t* = 127.5 seconds. *Right: t* = 129.5 seconds.

Fig. 15 shows the CVF and WSE for three simulation times. It can be seen how the inlet jet sweeps the whole conical reactor wall, raising the uppermost side of the cone and generating a rotational flow pattern evidenced by a significant wake. As was expected the maximum CVF are found just at the opposite wall respect to the inlet jet direction. However, the particle residence time at cone wall is controlled by the spout rotational speed, being for this case (10 rpm) less than 2 seconds. Graphics in Fig. 16 display the maximum and minimum CVF and WSE over the conical reactor walls for all analyzed re-circulation flows. As regard maximum CVF values, they hold between $3.5x10^{-4}$ and $5x10^{-4}$ but, as it was previously mentioned, particles are continuously removed from the cone wall. Moreover minimum CVF are roughly constants along the radius, with values around $2.5x10^{-4}$. As for the maximum WSE, a marked increasing is founded. For the highest re-circulation flow maximum WSE upper than 50 Pa are obtained until radius close to 1 m. Even at the uppermost point of the conical reactor wall the maximum WSE values can reach value rounding 10 Pa.

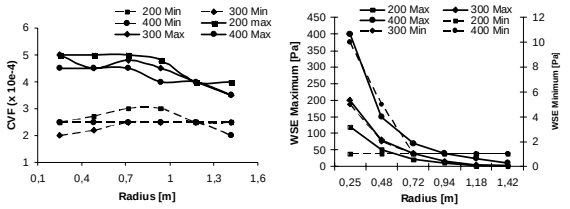

Fig. 16. Maximum and minimum CVF and WSE over the conical reactor walls for the three analyzed flows. *Left:* CVF. *Right:* WSE.

III. CONCLUSIONS

The numerical analysis carried out in the present study reached to the following conclusions:

- Under actual operation conditions an increase in catalyst particle concentration is evidenced over the conical reactor walls. Moreover, low wall shear efforts are also founded.
- Simulations show that the re-circulated inlet flow is strongly channeled over a small fraction of the overall conical reactor wall. This fact produces lower wall shear efforts over the opposite wall, increasing catalyst concentration. Increasing the re-circulation flow does not modify this flow pattern.
- A remarkable improvement is obtained by removal the inlet elbow, incorporating a rhomboidal flow deflector inside the reactor and increasing the re-circulation flow. This enhancement quickly diminishes far from the deflector zone.
- Finally, higher wall shear efforts and lower catalyst concentrations are obtained by incorporating a gyratory spout to inject the re-circulation flow. It produces a high-velocity inlet jet that sweeps the whole conical reactor wall in each spin.

IV. ACKNOWLEDGEMENTS

This work was supported by Centro de Tecnología Argentina (CTA) of Repsol-YPF, Complejo Industrial Ensenada (CIE) (SAT-Exp UNL 485789), Concejo Nacional de Investigaciones Científicas y Técnicas (CONICET, Argentina, grant PIP 5271), Universidad Nacional del Litoral (UNL, CAI+D 2005-10-64) and ANPCyT (Argentina, grants PICT 12-14573/2003 (Lambda), PME 209/2003 (Cluster) and PID 398/03 (DIVA)).

REFERENCES

Kennedy P.J. and Marechal E., "Carbocationic Polymerization", Krieger Publishing Company (1991).

Ranade V., "Computational flow modeling for chemical reactor engineering", Academic Press (2002).

Enwald H., Peirano E. and Almstedt A.,"Eulerian two-phase flow theory applied to fluidization", *Int. J. Multiphase Flow*, **22**, 21-66 (1996).

Srivastava A. and Sundaresan S., "Analysis of a frictional–kinetic model for gas–particle flow", *Powder Technology*, **129**, 72-85 (2003).

Makkawi Y. and Ocone R., "Modelling the Particle Stress at the Dilute-intermediate-dense Flow Regimes: A Review", *Chemical Engineering, School of Engineering and Physical Sciences*, Heriot-Watt University (2003).

Gidaspow D., Jung J. and Singh R., "Hydrodynamics of fluidization using kinetic theory: an emerging paradigm 2002 Flour Daniel lecture", *Powder Technology*, **148**, 123-141 (2004).

Smagorinsky, J., "General circulation experiments with the primitive equations: I. the basic equations". *Mon. Weather Rev.*, **91**, 99-164 (1963).

Wilcox, D., Turbulence Modeling for CFD, 2nd ed. DCW. ISBN: 0963605151 (1998).

Tezduyar, T., Mittal, S., Ray, S., and Shih, R., "Incompressible flow computations with stabilized bilinear and linear equal order interpolation velocity-pressure elements". *Computer Methods in Applied Mechanics and Engineering*, **95**, 221-242 (1992).

García-Cascales J. and Paillère H., "Application of AUSM schemes to multi-dimensional compressible two-phase flow problems", *Nuclear Engineering and Design*, **236**, 1225-1239 (2006).

Zanotti A., "Modelado del flujo multifase en la producción de acero por colada continua", PhD thesis, Facultad de Ingeniería y Ciencias Hídricas, Universidad Nacional del Litoral, Santa Fe, Argentina (2007).

Storti M, Nigro N. and Paz R., "PETSc-FEM a general purpose, parallel, multy-physics fem program". International Center of Computational Method in Engineering (CIMEC), Argentina http://www.cimec.org.ar/petscfem

Sonzogni, V., Yommi, A., Nigro, N., and Storti, M., "A parallel finite element program on a Beowulf Cluster", *Advances in Engineering Software*, **33**, 427-443 (2002).